Metrol. Meas. Syst., Vol. 28 (2021) No. 2, pp. 323–342
DOI: 10.24425/mms.2021.136610

PAN POLSKA AKADEMIA NAUK

METROLOGY AND MEASUREMENT SYSTEMS
Index 330930, ISSN 0860-8229
www.metrology.wat.edu.pl

M&MS

RECONSTRUCTION OF SMALL COMPONENTS USING PHOTOGRAMMETRY: A QUANTITATIVE ANALYSIS OF THE DEPTH OF FIELD INFLUENCE USING A MINIATURE STEP GAUGE

Maria Grazia Guerra[1)], Luigi Maria Galantucci[1)], Fulvio Lavecchia[1)], Leonardo De Chiffre[2)]

1) *Politecnico di Bari, Department of Mechanics, Mathematics and Management, via E. Orabona 4, 70126 Bari, Italy* (✉ *mariagrazia.guerra@poliba.it*, +39 3462 408 184, *luigimaria.galantucci@poliba.it*, *fulvio.lavecchia@poliba.it*)
2) *Technical University of Denmark, Department of Mechanical Engineering, Produktionstorvet 425, DK-2800 Kgs. Lyngby, Denmark* (*ldch@mek.dtu.dk*)

Abstract

In this work, authors investigated the effect of the Depth of Field (DoF) reduction, arising when the acquisition of small objects is carried out with a photogrammetry-based system using a Digital Single Lens Reflex (DSLR) camera and the structure from motion (SfM) algorithm. This kind of measuring instrument is very promising for industrial metrology according to the paradigms of the fourth industrial revolution. However, when increasing the magnification level, necessary for the reconstruction of sub-millimetric features, there is a corresponding decrease of the DoF, leading to possible effects on the reconstruction accuracy. Thus, the effect of the DoF reduction was analysed through the reconstruction of a well-known artefact: the step gauge. The analysis was conducted considering the theory behind the DoF concept, the analysis of the 2D images, input of photogrammetric reconstruction and, finally, the results in terms of dimensional verification of the reconstructed step gauge.

Keywords: metrology of small parts, uncertainty, photogrammetry, depth of field, miniature step gauge, flatness, dimensional accuracy.

1. Introduction

The implementation of the close-range photogrammetric technique largely increased in the last years and it involves several fields of application with successful results [1, 2]. Due to great applicability of this technique, objects with different characteristics, in terms of texture (visible and tactile) and geometrical complexity, have been reconstructed, pointing out its main difficulties and potentialities. Photogrammetry turn out to be a valid and reliable technique for creating 3D models of museum artefacts showing different optical properties (absorptivity, reflectivity, scattering), challenging texture and complex shape/geometry [3]. Moreover, great interest is

Article history: received September 8, 2020; revised November 9, 2020; accepted January 11, 2021; available online March 19, 2021.

emerging from industrial manufacturing thanks to more recent results obtained when measuring small components with good accuracy and low uncertainties [4–7]. At present, there are also other techniques able to measure features at the micro-scale level, however, limitations exist [8]. Micro-coordinate measuring machines are able to measure objects with very low uncertainties, but for highly complex parts there are at least two unsolved issues: the time needed for acquiring a sufficient number of points and the accessibility of some surfaces. On the other hand, 3D optical techniques [9] enable measuring large amounts of points within a single measurement, even in the presence of freeform geometries. Among these, photogrammetry has significant benefits, since, considering certain configurations and applications, it represents a simple, low-cost and versatile technique for measuring different geometries and materials. When photogrammetry is applied to scanning small objects, the use of zoom and macro lenses is needed in order to reach both proper magnification level and resolution. Nevertheless, when increasing the magnification level, there is a corresponding decrease of the *Depth of Field* (DoF) of the captured images, leading to a decrease of the reconstruction quality. The DoF limitations are, then, more significant when dealing with measurement of micrometric features. Since only a small portion of the image appears sharp enough to be used for 3D reconstruction, the image matching algorithms work badly on blurred areas and the first consequence is a reduction of the number of reconstructed points [10], as well as, the increase of the noise level, with more topological errors [11].

Several methods are used to tackle the problems related to the DoF and the loss of contrast due to diffraction [12]. In [13] a multistack procedure was developed using a Cartesian acquisition strategy, while in [10] a multi-view stereo and an image fusion technique was developed and tested for reconstructing archaeological artefacts. In [14] a focus stacking procedure was applied for reconstruction of small fossil teeth, and in [15] a similar method was also used for reconstruction and archiving of insects models. Other methods for extending the DoF were found and tested in [16], where the Scheimpflug rule was applied in order to adapt the DoF to the subject of interest. The specific lenses, used for this purpose [16], allow inclining the optical axis to modify the DoF: they are called tilt-shift lenses.

DoF reduction occurring when certain optical configurations are implemented is a discussed topic in literature, although it has not been quantitatively assessed how it affects the quality of reconstruction of a photogrammetry-based system in a more metrological context. A very simple way of conducting a quantitative analysis of the effects of the DoF reduction phenomenon is to use properly chosen reference objects. In this case the selected geometry was the *step gauge*. It has been already successfully tested in a general assessment of 3D laser scanners [17], as well as, for the sub-surface scattering evaluation of 3D optical scanners [18] and, generally, the evaluation of optical interactions due to the translucency of some materials. This is possible, thanks to the simultaneous presence of unidirectional and bidirectional lengths, allowing the detection of effects not observed when simpler geometries, such as spheres or gauge blocks, are used. Moreover, it is not a complex geometry and it can be easily calibrated using a fully traceable *Coordinate Measuring Machine* (CMM).

In this paper, a miniature step gauge made of *Polyphenylene Sulphide* (PPS) [19], was used to evaluate the DoF influence. The choice of the PPS material is due to the great use of polymers in the manufacturing industry, increasing the interest in testing the capabilities of available measuring instruments when dealing with problematic materials. Moreover, it was interesting for the authors to evaluate in this paper the effect of the DoF reduction not only on the 2D images, but mostly on the 3D reconstructed models. For this purpose, a testing object was necessary with structured features, such as the step gauge grooves.

The present work is motivated by a great and increasing interest towards the use of photogrammetry for the reconstruction and measurement of small artefacts in different fields, including the

Metrol. Meas. Syst., Vol. 28 (2021), No. 2, pp. 323–342
DOI: 10.24425/mms.2021.136610

industry. With this aim, a well-known and already implemented scanning system, as well as, a well-known reference object, have been used in order to quantify, for the first time and in a more rigours and structured way, the effect of the DoF on the photogrammetric reconstruction of small objects.

In this paper there is a section dedicated to the Materials and Methods adopted, describing the reference object, the measuring equipment and the data analysis procedures. Then, results of the proposed analysis will be reported in the dedicated sections, followed by their discussion.

2. Materials and methods

2.1. Step gauge

Step gauges are typically obtained by assembling gauge blocks made of steel or ceramics. The step gauge geometry is well suited for detecting and correcting systematic deviations since it features unidirectional as well as bidirectional lengths [20]. The former are suitable for scale correction and they can be used for assessing the accuracy of a measuring system. Bidirectional lengths take into account the "probing" effect and they can be used for detecting effects because of the interaction between the measuring instrument and the optical properties of the measured part [18]. The overall geometry of the step gauge used in this work is shown in Fig. 1, with dimensions of $58 \times 8 \times 7$ mm^3, including 11 grooves with 2 mm of depth and width. Referring to studies on Computed Tomography [21], PPS with 40% of glass was found to be a good material for a step gauge, featuring low form errors, similar to those obtained using aluminium and steel, good thermal stability, low density, and acceptable surface cooperativeness. A PPS miniature step gauge was thus used in this work. The unidirectional lengths previously calibrated through a traceable CMM were used for the computation of the scale factor. In Fig. 1, the step gauge geometry and the graphical meaning of unidirectional and bidirectional lengths, L_{Um} and L_{Bm}, respectively, are illustrated, see (1) and (2).

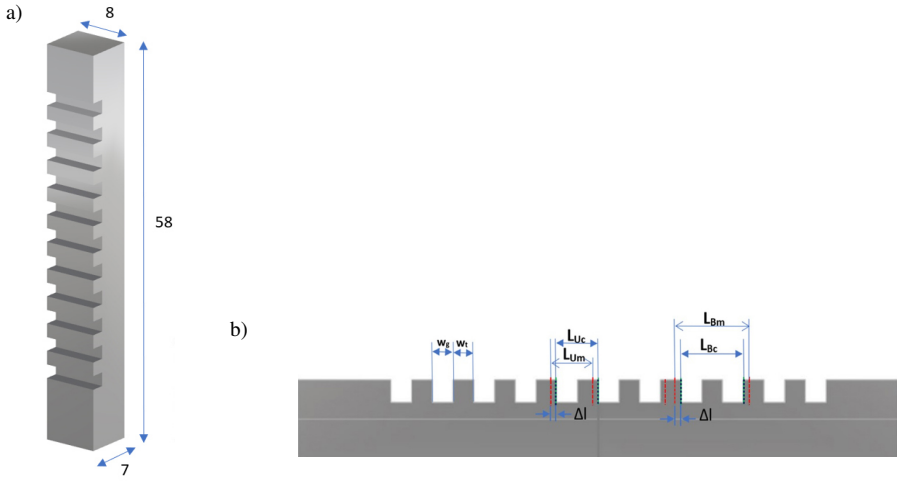

Fig. 1. Step gauge geometry and overall dimensions expressed in mm (a) unidirectional and bidirectional lengths definition (b).

$$L_{Um} = w_g + w_t - \Delta l + \Delta l\,, \tag{1}$$

$$L_{Bm} = w_g + w_t + \Delta l + \Delta l\,, \tag{2}$$

where:

L_{Bm} is the measured bidirectional length;
L_{Bc} is the calibrated bidirectional length with a contact probe;
L_{Um} is the measured unidirectional length;
L_{Uc} is the calibrated unidirectional length with a contact probe;
w_g is the groove width;
w_t is the tooth width;
Δl is the offset with respect to the real surface of the object.

In this study, the dimensional verification comprising the uncertainty assessment was carried out by measuring the unidirectional *Ui* and bidirectional lengths *Bi*, shown in Fig. 2.

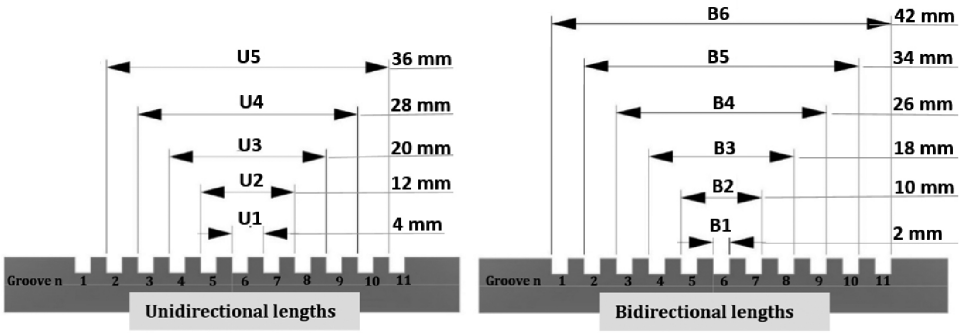

Fig. 2. Measurands description. The nominal value of each length is shown.

The step gauge was previously calibrated with a CMM Zeiss OMC 850 equipped with a probe ø 0.8 mm. Measures are shown in Table 1 with the associate expanded uncertainty (U), computed according to the ISO 14253-2 (ISO 14253-2:2011, 2011).

Table 1. Step gauge calibrated lengths.

Bidirectional Lengths	Length [mm]	U [mm]	Unidirectional Lengths	Length [mm]	U [mm]
B1	1.997	0.0008	U1	3.999	0.0020
B2	9.999	0.0008	U2	11.997	0.0011
B3	17.999	0.0012	U3	19.995	0.0013
B4	25.996	0.0019	U4	27.994	0.0019
B5	33.996	0.0022	U5	35.994	0.0022
B6	41.998	0.0026			

2.2. Photogrammetric hardware and software

The experiments were conducted using a *Canon EOS 760D* Digital SLR camera (24.2 Mpx, Sensor size APS-C 22.2 × 14.8 mm) equipped with a *Canon EF 50 mm f/1.8 II* lens and *Kenko Extension Tubes*. The focal length was a fixed one (50 mm) focused to infinity and three different extension tubes were applied in order to change the magnification level. In equation (3), the

presence of extension tubes is accounted for through the focusing distance (d) parameter, which changes according to the extension tube applied. In particular, the shorter the extension tube, the bigger is the focusing distance.

The camera is part of a completely motorized and automated 3-axe (ρ, ψ, θ) system numerically controlled by a computer, realized and called by the authors *Photogrammetric Scanning System with a Rotary Table* (PSSRT) described in detail in [22] and shown in Fig. 3. With the PSSRT the object is placed on a rotary table (T – θ angle), while the Digital SLR camera (C) is fixed on a rigid support moving along a linear axis (R – ρ), in order to regulate the focusing distance (fixing the focusing position to infinity and mounting an extension tube for the selected extension). Another controlled axis allows the regulation of the camera tilt angle (ψ), rotating the entire structure on which the camera is mounted. The third axis is the rotary table (θ axis), on which an integrated LED lightning system ensures homogeneous lighting conditions during the rotation. The movement on each axis is provided by stepper motors and measured by encoders. The resolution of the motorized system is 0.001 mm on ρ, 0.004° on ψ, and 0.18° on θ. The shooting command of the camera is also controlled by the computerised system.

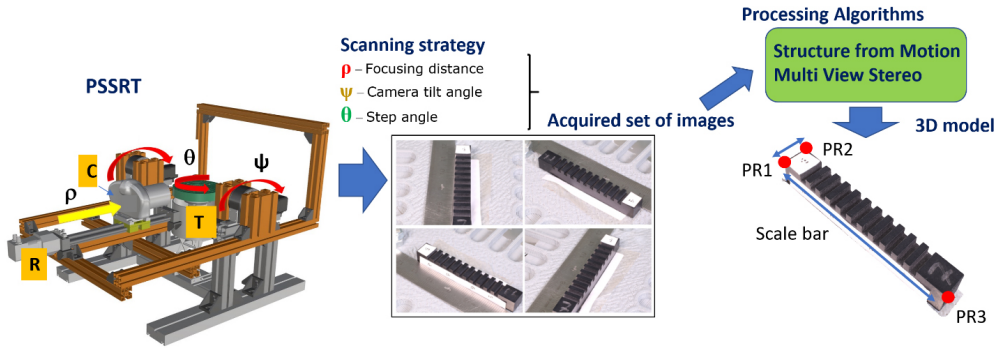

Fig. 3. Workflow of the photogrammetric reconstruction process, from the acquisition of images with the PSSRT to the 3D reconstructed model.

Only fixed focal lenses are used, having so fixed the focus at known distances (d) adjusted regulating the position of the camera with respect to the object through the sliding platform (R). The tilt angle (ψ) can be regulated according to the slope of the surfaces of the scanned object, increasing this angle, if there is a prevalence of horizontal surfaces, or, decreasing it, if there is a prevalence of vertical surfaces. Once the equipment is set and fixed, the scan can be carried out automatically acquiring pictures during a complete rotation of the table (360°). The rotation step angle between each shot (θ) is another important process parameter: with reducing the step angle, a higher number of pictures is taken with higher overlapping, at the expense of an increase of time required for scanning and computer processing. Thus, in the presented system, step angle (θ), tilt angle (ψ) and focusing distance (ρ) describe the scanning strategy.

In particular, in this work, two tilt angle values, (ψ = 45° and ψ = 60°), both suitable for the acquisition of the step gauge geometry (the groove sides were visible in both configurations), were used and their effects evaluated. The number of captured images for each configuration was 72, which means a rotation step of 5° of the rotary table.

The image processing, the core of the photogrammetric reconstruction, was carried out with the Agisoft Photoscan commercial software (for this study, version 1.4.4 was used). It is based on

Structure-from-Motion (SFM) and on *Multi-View Stereo* (MVS) principles. The basic workflow of the system used is illustrated in Fig. 3.

The processing parameters used in Agisoft Photoscan v.1.4.4 were set for all phases (alignment, dense cloud generation and mesh generation) to high quality, in order to exploit the full resolution of the acquired images, while the camera calibration was conducted directly from the step gauge pictures during the alignment phase.

The scaling process was carried out in two stages. At first, a scale factor was computed choosing three reference points on the step gauge whose distances had previously been measured.

Afterwards, in order to refine the scaling process, considering possible errors during the definition of the reference points on the images (user-dependency) and avoid the influence of the scale error in the DoF analysis, the scale was adjusted through the use of the step gauge unidirectional lengths, threshold independent, widely implemented for scale error correction by using linear regression [23].

2.3. Depth of field model equation

Considering a lens focused on a subject, the DoF is defined as the region (range of distances) before and after the plane of focus within which subjects appear acceptably sharp on the image. Outside this region, there is a progressive loss of details and the image becomes blurry. The DoF of a captured image is usually computed through an equation, which involves a set of parameters characterizing the selected optical configuration, as reported in (3). In particular, if the lens is focused to infinity, the DoF is influenced by the focal length (f), the camera aperture expressed as f-*stop* value (A), the object distance (d) and the circle of confusion (c) [24]. A graphical representation is shown in Fig. 4.

$$\mathrm{DoF} = \frac{2df^2Ac(d-f)}{f^4 - (Ac(d-f))^2}, \tag{3}$$

where:

f is the focal length;

A is the aperture of the camera, expressed as f-*stop* value;

d is the object distance;

c is the circle of confusion.

Regarding the circle of confusion, there are many issues related to the computation of this parameter. Due to its great influence in the computation of DoF value, in this work it was considered as the *Airy disk* (AD) value [25]. As reported in [26], when considering a specific camera/lens configuration, the diffraction limit has to be considered, and, as a consequence, value c should not be smaller than the size of the AD. The size of the AD is a function of the effective aperture (E) and of the light wavelength, according to (4).

$$AD = 2.44 \times \lambda \times E, \tag{4}$$

where: λ is the wavelength of light considered; E is the effective aperture, which is function of the magnification level (M) and of the camera aperture expressed as f-*stop* value (A), see (5):

$$E = A \times (M + 1). \tag{5}$$

Since in the analysed case photogrammetry uses the visible spectrum of light, the value was set to 580 nm. However, the visible light wavelengths range between 405 nm (violet) and 880 nm (near-infrared).

Metrol. Meas. Syst., Vol. 28 (2021), No. 2, pp. 323–342
DOI: 10.24425/mms.2021.136610

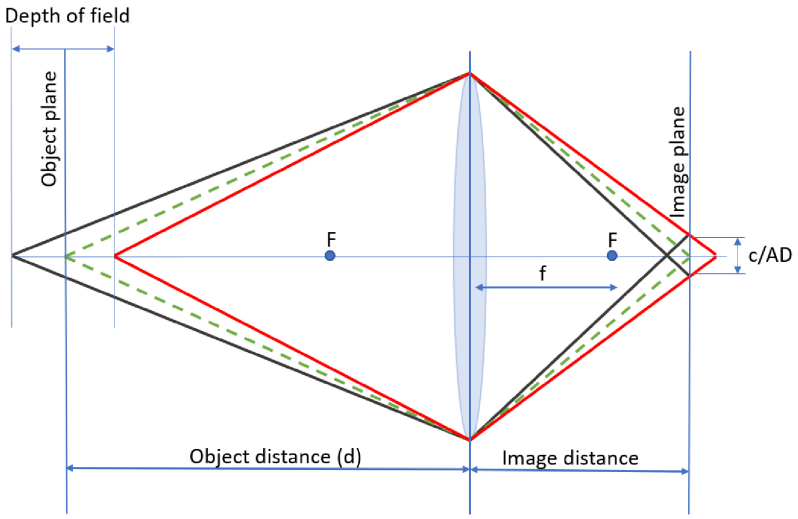

Fig. 4. Depth of field graphical representation.

Thus, the *AD* values were computed within the range of visible light (λ_1 = 405 nm, λ_2 = 580 nm, λ_3 = 880 nm) and they are shown in Table 2.

Table 2. Airy Disk values according to the considered magnification level and the light wavelengths, the *f-stop* considered was 20.

Optical config.	***M* level**	***f-stop value* (*A*)**	***AD*(λ1) [mm]**	***AD*(λ2) [mm]**	***AD*(λ3) [mm]**
M1	0.24×	20	0.025	0.035	0.053
M2	0.4×	20	0.028	0.040	0.060
M3	0.64×	20	0.033	0.046	0.070

The *f-stop* value (*A*) used in this specific case was 20. Similar values were used in previous researches [22, 27] where photogrammetry-based systems were used for metrological purposes of measuring sub-millimeters features. The choice was made in order to maximize the DoF.

In Fig. 5a, the obtained DoF values, computed according to different light wavelengths and different magnification levels *Mi*, are shown, keeping the *f-stop* value fixed at 20 (which was the used *f-stop* value in this paper). As can be seen in Fig. 5b, instead, the DoF was computed using different f-stop values (from 12 to 20), and, for ease of reading, it was considered just the average visible light wavelength (λ_2 = 580 nm).

2.4. Experimental set-up

With the equipment described in the previous sections (photogrammetric hardware and software), the considered step gauge made of PPS was acquired with five repetitions and then reconstructed using the optical configurations shown in Table 3. In particular, all the magnifications were achieved combining the 50 mm lens with different extension tubes: 12 mm for M1, 20 mm for M2 and 32 mm for M3.

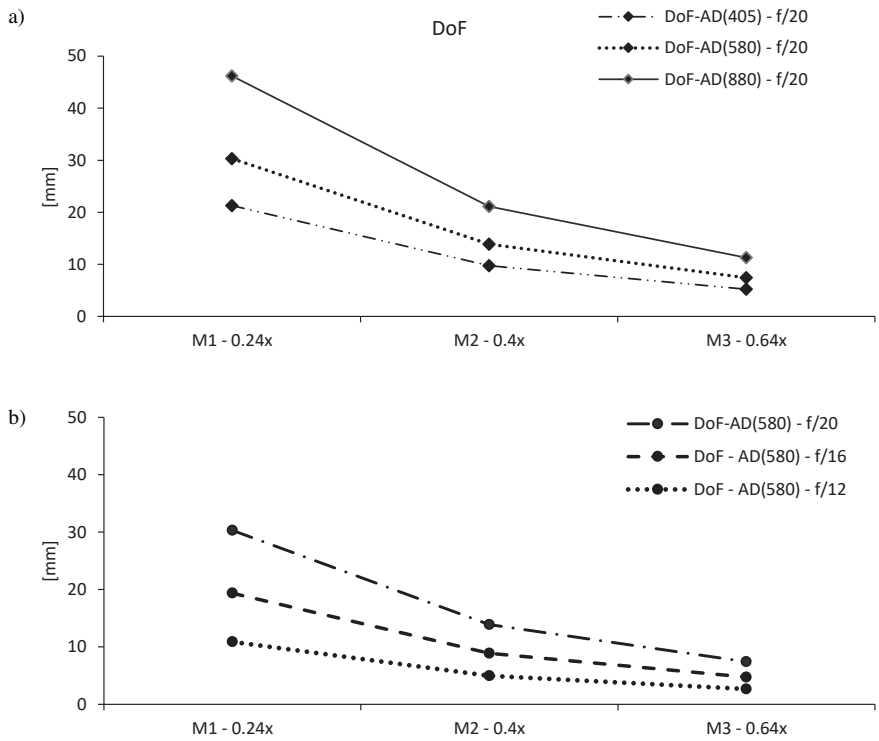

Fig. 5. DoF values according to different light wavelengths and different magnification levels Mi (a). DoF trend according to different Mi, using the AD (λ_2 = 580 nm) and changing the *f-stop* value (b).

Table 3. Experimental plan and number of tests.

	tilt angle		Number of tests
Optical configuration	45°	60°	
M1 0.24×	5 repetitions	5 repetitions	10
M2 0.4×	5 repetitions	5 repetitions	10
M3 0.64×	5 repetitions	5 repetitions	10
Total number of tests	15	15	30

Regarding the scanning strategy, the reason for using two different tilt angle values is that this factor combined with the object geometry (slope) can change the *in-focus depth* value, or in other terms, the portion of the object actually in focus. In Fig. 6, two cases are shown: one with the optical axis of the camera orthogonal with respect to the object plane (a), the other with the same axis tilted at a certain angle with respect to the object plane (b). This example shows how the tilt angle (ψ) changes the portion of the object actually in focus. This portion will be indicated with the term *in-focus depth*. Thus, according to Fig. 6 and using (6), it is possible to compute its value, depending on the chosen ψ value.

$$\textit{In-focus depth}\,(\psi) = \text{DoF [mm]}/\cos(\psi). \tag{6}$$

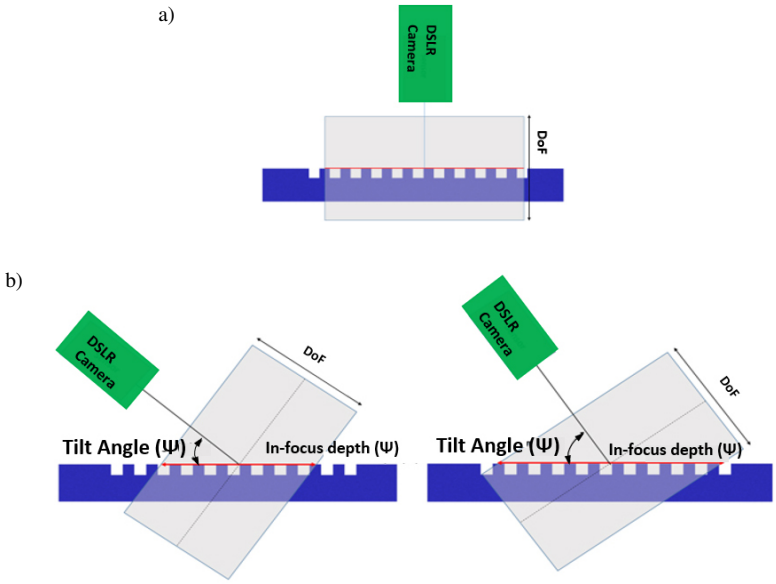

Fig. 6. Sensor tilt angle and in-focus depth when the optical axis is orthogonal to the object plane (a) and when is tilted at a certain angle (b).

2.5. Data analysis

The analysis was conducted in different steps.

Firstly, images, the fundamental input of photogrammetric reconstruction, were filtered and analysed in order to understand how the DoF affects each captured image. Through the application of specific image filters, such as edge detection filters, it is possible, as found in literature [28], to detect the in-focus area of a captured image, starting from the consideration that, after converting into greyscale, images containing sharp edges result in higher grey values. When the image is blurred, the gradient is low [29].

The dimensional verification, comprising the uncertainty assessment, was carried out by measuring the unidirectional *Ui* and bidirectional lengths *Bi*, as shown in Fig. 2. As the index *i* increases, the lengths involve groove sides far from the focusing point (which is placed at the centre of the step gauge, approximately at roove 6) and they are more affected by the limited DoF.

The uncertainty evaluation of the PSSRT was conducted according to the ISO 14253-2 (ISO 14253-2:2011, 2011). The uncertainty contributors are reported in Table 3 and the confidence level is set to 95%, corresponding to a coverage factor *k* equal to 2.

The general equation is:

$$U = kx\sqrt{u_r^2 + u_w^2 + u_e^2 + u_p^2}\,. \tag{7}$$

The uncertainty assessment was carried out considering the uncertainty components reported in Table 4.

Starting from the general equation, the reference uncertainty was considered as the uncertainty of calibration of each single unidirectional and bidirectional length. The component due to the environmental temperature was also accounted for and the uncertainty due to the repeatability was computed considering five repetitions.

Table 4. Uncertainty budget.

Uncertainty contributor category	Symbol	Type	Estimation	Distribution	Uncertainty contributor
Reference	u_r	B	Reference Uncertainty	Rectangular	$U_i/\sqrt{3}$
					With i representing each measurand
Optical interaction scanner/workpiece	u_w	A	Fitting Error	Rectangular	σ *fit* error
Environment	u_e	B	Temperature variation	U-shaped	±1°C
Procedure	u_p	A	Repeated measurements	Normal	$\sigma_{PSSRT}\sqrt{n}$
					With σ the standard deviation of n repetitions

The step gauge is a calibrated test object with a low form error (about 1–2 μm) and low roughness values (Ra = 0.82 μm), evaluated on the groove sides from which the measurands are defined. As a consequence, any deviation from ideal geometry found on the 3D reconstructed models is not attributable to the step gauge itself, but it is possible to attribute this component to the reconstruction quality. Each step gauge side, included in the measurand definition (Fig. 2) was then fitted with a plane through the *Least Square Method* (LSM). Thus, in order to relate the reconstruction quality with the uncertainty of measurement, the uncertainty component coming from the workpiece was considered as the standard deviation of the fitting error, σ *fit*, which is the standard deviation of orthogonal distances between given points (the obtained point cloud/mesh) and the ideal geometric feature fitted, describing the distribution of the points with respect to the fitted plane [30]. The variability of the fitting error, σ *fit*, is a good indicator of the reconstruction quality since, the higher the variability of the points reconstructed, due to the optical interaction between the measurement system and the object surface, the worse the reconstruction quality.

By using the fitting error as quantitative description of the reconstruction quality, correspondences between the 2D image analysis and the 3D reconstruction quality were checked.

3. Results

3.1. 2D Image analysis

After theoretically computing the DoF for each involved configuration, an image analysis of the acquired images was conducted. In Figs. 7 and 8 images of the PPS step gauge acquired with configurations M1, M2 and M3 are shown before (original images) and after the application of the Sobel filter, using the freeware GIMP-GNU Image Manipulation Software (GIMP Team, 2019). Bright pixels represent the in-focus area, on the contrary, dark pixels are less in focus.

Through the visual inspection of the filtered images, it was possible to observe areas more in focus. Comparing these results with respect to values computed through (2), it was possible to observe that the image portion characterized by acceptable sharpness of details (in-focus depth) is comparable with the DoF values estimated in (1) using the Airy Disk AD as circle of confusion, as shown in Fig. 9.

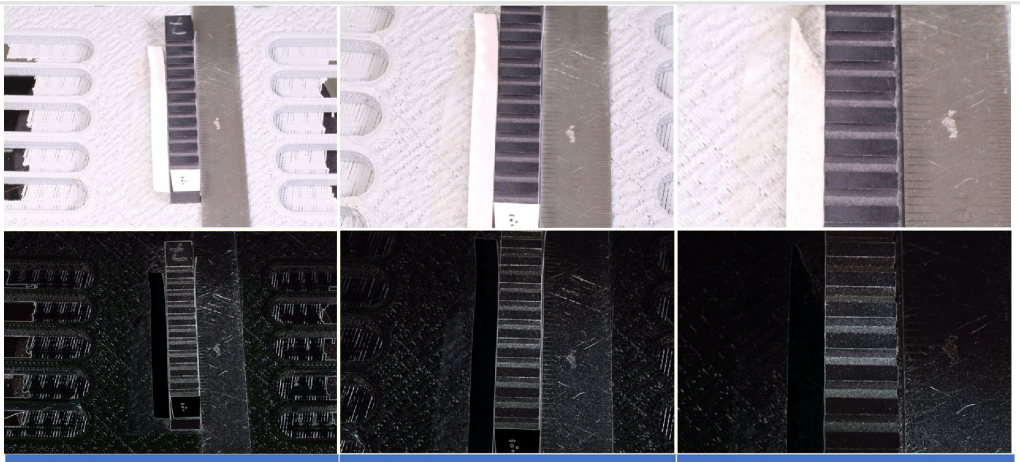

M1- ψ=60°		M2- ψ=60°		M3- ψ=60°	
Original image	Edge filter	Original image	Edge filter	Original image	Edge filter
Canon Eos 760D F-length: 50mm Ext-tubes 12 mm M: 0.24 Tilt Angle ψ: 60°	Edge detect Algorithm:Sobel Amount: 3 Border behaviour: Clamp	Canon Eos 760D F-length: 50mm Ext-tubes 20 mm M: 0.4 Tilt Angle ψ: 60°	Edge detect Algorithm:Sobel Amount: 3 Border behaviour: Clamp	Canon Eos 760D F-length: 50mm Ext-tubes 32 mm M: 0.64 Tilt Angle ψ: 60°	Edge detect Algorithm:Sobel Amount: 3 Border behaviour: Clamp

Fig. 7. Application of the Sobel edge filter to the first captured image for each configuration with $\psi = 60°$.

M1- ψ=45°		M2- ψ=45°		M3- ψ=45°	
Original image	Edge filter	Original image	Edge filter	Original image	Edge filter
Canon Eos 760D F-length: 50mm Ext-tubes: 12 mm M: 0.24 Tilt Angle ψ: 45°	Edge detect Algorithm:Sobel Amount: 3 Border behaviour: Clamp	Canon Eos 760D F-length: 50mm Ext-tubes: 20 mm M: 0.4 Tilt Angle ψ: 45°	Edge detect Algorithm:Sobel Amount: 3 Border behaviour: Clamp	Canon Eos 760D F-length: 50mm Ext-tubes: 32 mm M: 0.64 Tilt Angle ψ: 45°	Edge detect Algorithm:Sobel Amount: 3 Border behaviour: Clamp

Fig. 8. Application of the Sobel edge filter to the first captured image for each configuration with $\psi = 45°$.

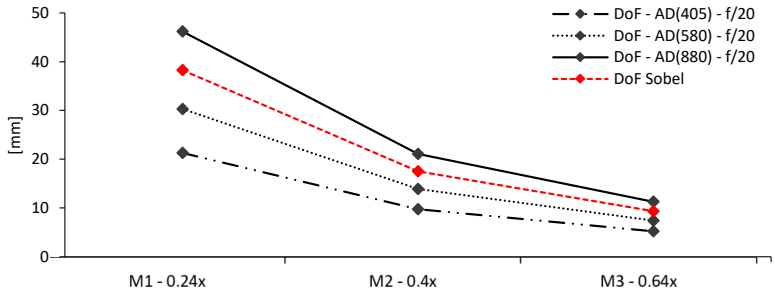

Fig. 9. DoF values obtained by image analysis (Sobel filter) compared with the ones computed through (1) with c computed as Airy Disk AD.

3.2. 3D reconstruction analysis

The acquired images were then processed by the Agisoft Photoscan software and results related to the 3D reconstructed models were reported in Table 5. Among them, the *ground sampling resolution* (GSD), expressed in mm/pixel and the average reprojection error are reported.

Table 5. Some parameters representative of the quality of 3D reconstructed models from the Agisoft Metashape report.

	M1	**M2**	**M3**
Ground Sampling Distance (GSD) [mm/pixel]	0.0155	0.0096	0.0063
Average Reprojection Error [pixel]	0.412	0.387	0.385

These data give a first insight into the quality of the reconstructed models and, according to the obtained values, the reconstructed models are suitable for further analysis. At this stage, no evident effects of the DoF reduction are identifiable from the reported data.

Afterwards, the resulting meshes were analysed with the GOM Inspect software.

Firstly, a reference system was set, and then, for each groove side a plane was fitted, through the least square method. The dimensional verification involved the measurement of both unidirectional and bidirectional lengths defined as distances between the planes fitted on the involved groove sides, respectively.

Results obtained from the dimensional verification are expressed in terms of average errors estimated on unidirectional and bidirectional lengths, as reported in (8).

$$error = x - x_{\mathrm{cal}}\,, \tag{8}$$

where: x is the photogrammetric measured value and x_{cal}, the calibrated value.

Unidirectional lengths. Errors evaluated on unidirectional lengths are shown in Fig. 10a and 10b for tilt angles 45° and 60°, respectively.

The first consideration is that the tilt angle set to 45° produced better results in comparison with the configuration at 60°, and it is valid for M1, M2 and M3. Considering the tilt angle set to 45°, and configurations M1 and M2, errors registered on unidirectional lengths are lay in the small range below 0.003 mm, and the same was valid for configuration M3 for U1, U2 and U3, while U4 and U5 registered higher errors up to 0.006 mm. Different values were found when the tilt angle was set to 60°. Errors registered for M1 were below 0.004 mm and those registered for

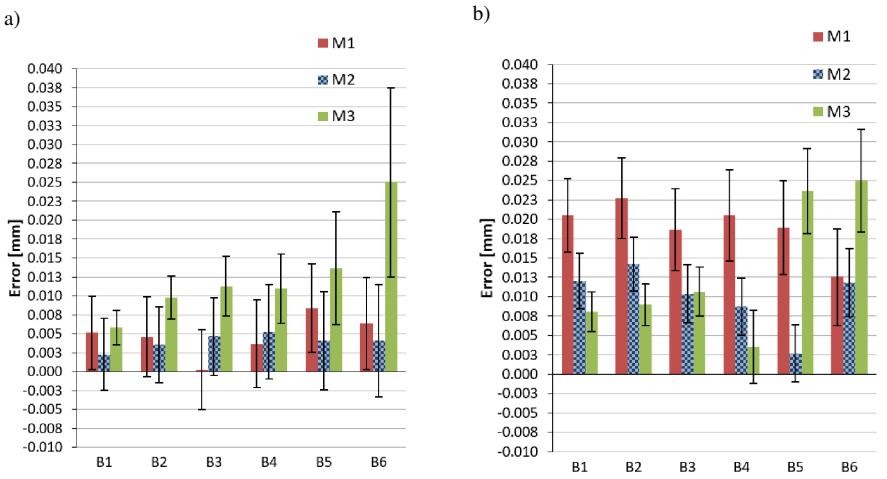

Fig. 10. Errors evaluated on unidirectional lengths [mm], considering the three configurations M1, M2 and M3 at tilt angle 45° (a) and tilt angle 60° (b).

M2 lay within 0.003 mm considering U1, U2 and U3 and with a marked tendency to increase up to 0.015 mm when considering U4 and U5. The same, more marked tendency, was found for configuration M3 with the highest errors registered for U4 and U5, up to 0.025 mm. Uncertainties represented in the form of error bars, were generally stable and higher for M1 when compared to M2 and M3, and they were on the order of 0.010 mm. Uncertainties characterizing M2 were slightly lower and they tended to increase from U1 to U5 and, in particular, from 0.009 mm (U1) to 0.012 mm (U5). The same was observed for configuration M3, where there was the maximum increase of uncertainty from 0.005 mm up to 0.01 mm. Thus, the uncertainties showed a tendency to increase when passing from the groove sides more in focus (U1, U2 and U3) to the ones less in focus (U4 and U5).

Bidirectional length. Regarding the bidirectional lengths, shown in Fig. 11a and 11b for tilt angles 45° and 60°, respectively, they registered higher errors as compared to unidirectional lengths and, generally, they were worse when considering the tilt angle 60°. Bidirectional lengths are more sensitive to many sources of error, such as subsurface scattering, thermal expansion, and, more generally, the "probing errors". Looking at the results, when the tilt angle is set to 45°, configuration M1 registered errors lay in the range between 0.004 mm and 0.009 mm. M2 was characterized by errors always below 0.005 mm, while M3 was characterized by an increasing trend between 0.006 mm and 0.025 mm (B6, including groove sides very far from the focusing point). Uncertainties were higher and almost constant for M1, slightly lower with a tendency to increase for M2 and lower with a more marked tendency to increase for M3. The same configurations, M1, M2 and M3 with a tilt angle set to 60° showed worse results. In particular, errors registered for M1 ranged between 0.013 mm and 0.023 mm. M2 was characterized by errors lay between 0.004 mm and 0.014 mm and, finally, M3 registered errors lay between 0.004 and 0.01 mm for the B1, B2, B3 and B4, while B5 and B6 were characterized by errors up to 0.025 mm. Even in this case, uncertainties were higher and almost stable for M1, slightly lower with a tendency to increase for M2 and lower with a more marked tendency to increase for M3.

As one can observe from the obtained results, the uncertainties were more affected by the DoF reduction when passing from configuration M1 to configuration M3. This is mainly due to the effect of the σ_{fit}, which was considered as an uncertainty component, as it well describes the

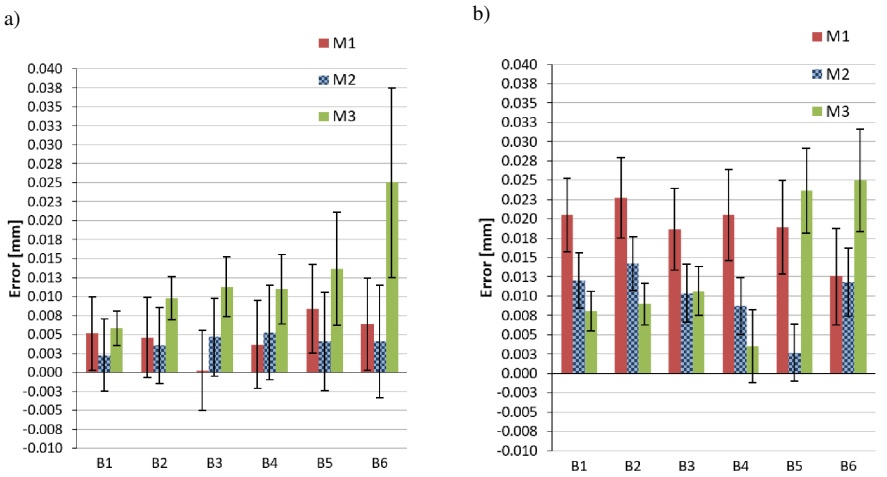

Fig. 11. Errors evaluated on bidirectional lengths [mm], considering the three configurations at tilt angles 45° (a) and 60° (b).

effect due to the interaction between the optical instrument and the object surface. The σ *fit* was evaluated for each groove side and it varied from groove 1 to groove 11. As can be seen in Fig. 12, for configuration M1, dots representing the σ *fit* values were randomly distributed for both tilt angle values, 45° and 60°. In these scanning configurations the in-focus depth detected using the Sobel filter covered more than the entire step of the gauge length. While the trend followed by the σ *fit* was parabolic for configurations M2 and M3.

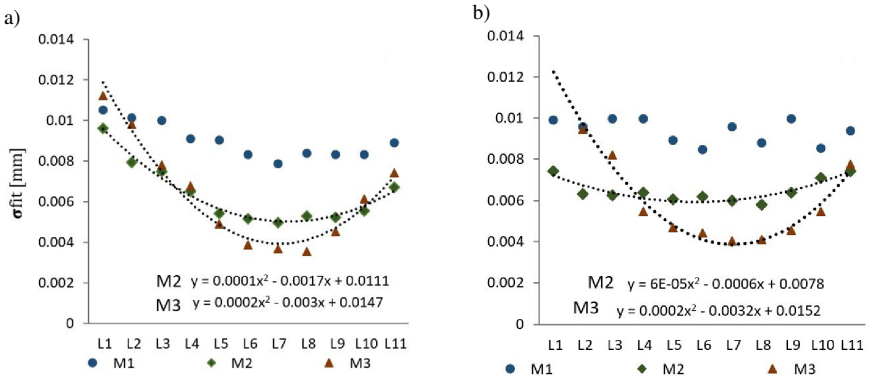

Fig. 12. Sigma fitting error trend for the tilt angles 45° (a) and 60° (b). Dot lines represent the fitted curves.

Observing configuration M2, a slight trend could be detected for the configuration at 45°, and it was well fitted by a parabola ($R^2 = 0.96$). The minimum of the parabola was detected in correspondence of grooves 6, 7 and 8. The highlighted effect is smoother for the configuration at 60°, characterized by a higher *in focus depth*, as stated in (6). Configuration M3 (0.64×) confirmed this tendency for both tilt angle values and, in more detail, the minimum of the parabola was reached in correspondence of groove sides 6, 7, 8 and 9.

Generally, models obtained using higher tilt angle values showed a wider portion of the object in focus, which was confirmed by larger parabolas, but the σ *fit* values, considering the same configuration, were lower at 45°, highlighting less variability of points and a better reconstruction quality. If those values are compared with the filtered images shown in Fig. 7 and Fig. 8, there is a good correspondence between the detected in focus depth and the groove sides characterized by the best reconstruction quality (lowest σ *fit*). The link between the trend followed by the σ *fit* and the in-focus depth detected after the application of the Sobel filter was further confirmed analysing the profile plots of the image and observing the grey value of each profile pixel (Fig. 13 and Fig. 14). After the application of the Sobel filter, the in-focus depth is characterized by bright pixels, while the blurred area by dark pixels. The profile plot shows how the grey value increases (white) when approaching the in-focus area of the image. In both cases (tilt angles 45° and 60°), the trend can be approximated by a parabola having an amplitude on the same order of magnitude as compared to the parabolas obtained considering the σ *fit*. The profile plots were obtained through the ImageJ software package (https://imagej.nih.gov/ij).

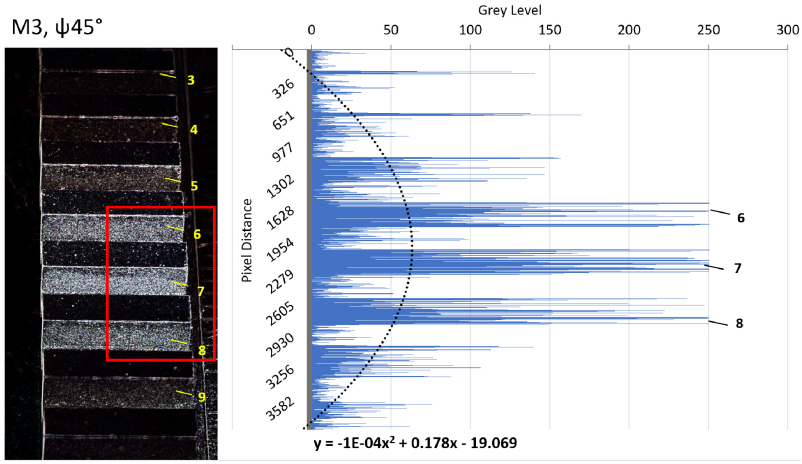

Fig. 13. Profile plot of the Sobel filtered image M3, $\psi = 45°$.

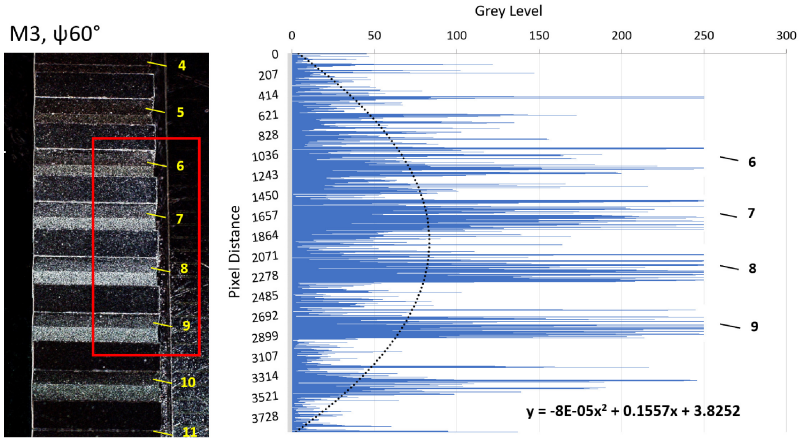

Fig. 14. Profile plot of the Sobel filtered image M3, $\psi = 60°$.

As it was observed, the effect on the quality of reconstruction, considered in the uncertainty computation as σ *fit*, exists and there is a close relation between the sharpness of details observed on the images and the reconstructed model.

It is important to stress here that the step gauge is a calibrated test object with a low roughness value (Ra = 0.82 μm) and flatness on the order of few micrometers. Thus, results obtained in these tests are not affected by manufacturing errors.

4. Discussion of results

Data obtained from the dimensional verification of the step gauge gave evidence to some aspects related to the influence of the DoF reduction when using a photogrammetry-based system for measuring small objects with high magnification levels. From the results analysed in the previous section, it was possible to observe how errors and uncertainty can vary according to the different configurations. In particular, the unidirectional lengths were more affected by the tendency to increase, especially for U4 and U5. Bidirectional lengths were apparently less affected by the same tendency, except for M3, but they are more sensitive to other sources of error, such as the subsurface scattering [18]. Uncertainties were more affected by the DoF, since they showed a clear tendency to increase for configurations M2 and M3 when moving far from the centre of the step gauge (the focusing point), for both considered tilt angle values. Moreover, from the previous sections, a good correspondence was found between the 2D filtered image data and the σ *fit* evaluated on the 3D reconstruction, as it was possible to observe from Fig. 13 and Fig. 14 (profile plots of the filtered images) when compared with Fig. 12 (σ *fit* trend). In order to better understand the behaviour of a photogrammetry-based system with respect to the DoF phenomenon, it is useful to observe the points detected on each captured image of the step gauge after the sparse cloud generation. This was possible in the Agisoft Photoscan software, enabling the visibility of the points recognized on each image. From Fig. 15, it is possible to observe that the points recognized on each image are divided in blue points and white points. Blue points are those having correspondence in at least two images in order to have the triangulation and they are called tie points. White points represent points recognized on one picture, so they do not contribute to the 3D model. The amount of detected tie points depends on several parameters:

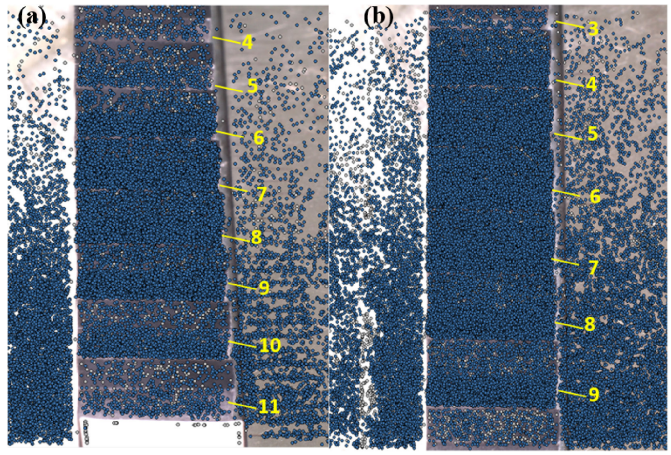

Fig. 15. Tie points detected on the first shot for configuration M3 at 45° (a) and 60° (b).

the kind of visible texture, the quality of the image and the sharpness of details of the image. It is possible to observe that the highest concentration of blue points is in the centre of the image corresponding to the more-in-focus area of the image. Thus, the correspondence found between the filtered 2D image and the form error in the 3D model is attributable to the different amount of points of acceptable quality that the system is capable to detect in each image.

As all the other optical scanners, Photogrammetry-based scanners, are greately influenced by the acquired surface characteristics (material and colour). This means that using another material would have produced different results in terms of numerical values of errors and uncertainty, especially if bidirectional lengths are considered. The only generalization possible, among the reported results, is the detected trend, which is not dependent on the specific object materials and colours but it is affected on the DoF decrease from the focusing plane to the peripheral areas. Generally, the effect of the DoF could be accounted for in the uncertainty of measurement if the σ *fit* component, strictly related to the DoF reduction, is considered as an uncertainty contributor.

The present work is motivated by the great and increasing interest towards the use of photogrammetry for the reconstruction and measurement of small artefacts in different fields, including the industry. The main contribution of this paper is a first quantitative evaluation of the DoF reduction occurring when a 3D measuring system based on photogrammetry is used for the reconstruction of small objects in a metrological context. With this aim, a well known and already implemented scanning system, together with a well known reference object, were used in order to quantify, in a more rigours and structured way, the effect of the DoF on the photogrammetric reconstruction of small objects. The step gauge geometry, indeed, was an effective reference object for this task, thanks to its step structure which allowed the detection of the data trend.

5. Conclusions

In this paper, the influence of the DoF reduction when using a photogrammetry-based system with high magnification levels was analysed and evaluated. The step gauge geometry resulted to be suitable for the investigation: the structured geometry allowed to analyse the DoF effects both on 2D images and directly on the 3D reconstructed models.

The analysis was conducted considering three optical configurations, leading to three different DoF values, and two different values of the sensor tilt angle, which changes the in-focus depth, according to the reconstructed geometry.

From the obtained results, configurations M2 (0.4×) and M3 (0.64×) were, as expected, more affected and they showed an increase of errors corresponding to the lengths involving the most peripheral sides of the step gauge, the ones less in focus. Generally, the effect of the DoF could be accounted for by the uncertainty of measurement if the σ *fit* component, strictly related to the DoF reduction, is considered as an uncertainty contributor.

When increasing the magnification level, (configurations M2 and M3), the σ *fit* followed a trend well fitted by a parabola, and the groove sides, placed in correspondence of the most in focus area of the step gauge, showed a lower σ *fit* value than the others. The effect was more relevant for the sensor tilt angle 45° and it is explained by the fact that at 45°, the portion of the object covered by the DoF is less than the portion of the object covered when the sensor is tilted at 60°. Despite the trend, more marked for the configuration at 45°, this configuration showed better results in terms of absolute values of errors and uncertainties since it is more suitable for acquiring the step gauge geometry, due to better visibility of the groove sides. This fact highlights that, despite the DoF, the scanning strategy must be decided according to the object geometry and 60° of tilt angle is not ideal for reconstructing highly sloped surfaces. Further reaearch

will be conducted considering other conditions, such as different camera aperture and different materials. Moreover, the effect of the selected acquisition parameters on spatial resolution, will be investigated.

Acknowledgements

This work was supported by the Italian Ministry of Education, University and Research under the Programme "Department of Excellence" Legge 232/2016 (Grant No. CUP – D94I18000260001).

References

[1] Maté-González, M. Á., Aramendi, J., Yravedra, J., Blasco, R., Rosell, J., González-Aguilera, D., & DomÍnguez-Rodrigo, M. (2017). Assessment of statistical agreement of three techniques for the study of cut marks: 3D digital microscope, laser scanning confocal microscopy and micro-photogrammetry. *Journal of Microscopy*, *267*(2), 356–370. https://doi.org/10.1111/jmi.12575

[2] Toschi, I., Capra, A., Luca, L. De, Angelo Beraldin, J., & Cournoyer, L. (2014). On the evaluation of photogrammetric methods for dense 3D surface reconstruction in a metrological context. *ISPRS Annals of the Photogrammetry, Remote Sensing and Spatial Information Sciences*, *2*(5), 371–378. https://doi.org/10.5194/isprsannals-II-5-371-2014

[3] Sapirstein, P. (2018). A high-precision photogrammetric recording system for small artifacts. *Journal of Cultural Heritage*, *31*, 33–45. https://doi.org/10.1016/j.culher.2017.10.011

[4] Galantucci, L. M., Guerra, M. G., & Lavecchia, F. (2018). Photogrammetry Applied to Small and Micro Scaled Objects: A Review. *Lecture Notes in Mechanical Engineering*, *0*(9783319895628), 57–77. https://doi.org/10.1007/978-3-319-89563-5_4

[5] Leach, R., Sims-Waterhouse, D., Medeossi, F., Savio, E., Carmignato, S., & Su, R. (2018). Fusion of photogrammetry and coherence scanning interferometry data for all-optical coordinate measurement. *CIRP Annals*, *67*(1), 599–602. https://doi.org/10.1016/j.cirp.2018.04.043

[6] Percoco, G., Guerra, M. G., Sanchez-Salmeron, A.-J., & Galantucci, L. M. (2017). Experimental investigation on camera calibration for 3D photogrammetric scanning of micro-features for micrometric resolution. *International Journal of Advanced Manufacturing Technology*, *91*(9–12), 2935–2947.

[7] Sims-Waterhouse, D., Piano, S., & Leach, R. (2017). Verification of micro-scale photogrammetry for smooth three-dimensional object measurement. *Measurement Science and Technology*, *28*(5). https://doi.org/10.1088/1361-6501/aa6364

[8] Dai, G., Neugebauer, M., Stein, M., Bütefisch, S., & Neuschaefer-Rube, U. (2016). Overview of 3D Micro- and Nanocoordinate Metrology at PTB. *Applied Sciences*, *6*(9), 257. https://doi.org/10.3390/app6090257

[9] Beraldin, J. A., Mackinnon, D., & Cournoyer, L. (2015). Metrological characterization of 3D imaging systems: progress report on standards developments. *International Congress of Metrology*, *3*, 1–21. https://doi.org/10.1051/metrology/20150013003

[10] Gallo, A., Muzzupappa, M., & Bruno, F. (2014). 3D reconstruction of small sized objects from a sequence of multi-focused images. *Journal of Cultural Heritage*, *15*(1), 173–182. https://doi.org/10.1016/j.culher.2013.04.009

[11] Nicolae, C., Nocerino, E., Menna, F., & Remondino, F. (2014). Photogrammetry applied to problematic artefacts. *ISPRS – International Archives of the Photogrammetry, Remote Sensing and Spatial Information Sciences*, *XL–5*(June), 451–456. https://doi.org/10.5194/isprsarchives-XL-5-451-2014

[12] Kuthirummal, S., Nagahara, H., Zhou, C., & Nayar, S. K. (2011). Flexible depth of field photography. *IEEE Transactions on Pattern Analysis and Machine Intelligence*, *33*(1), 58–71. https://doi.org/10.1109/TPAMI.2010.66

[13] Galantucci, L. M., Lavecchia, F., & Percoco, G. (2013). Multistack Close Range Photogrammetry for Low Cost Submillimeter Metrology. *Journal of Computing and Information Science in Engineering*, *13*(4), 044501. https://doi.org/10.1115/1.4024973

[14] Santella, M., & Milner, A. R. C. (2017). Coupling Focus Stacking with Photogrammetry to Illustrate Small Fossil Teeth. *Journal of Paleontological Techniques*, *18*(18), 1–17.

[15] Ströbel, B., Schmelzle, S., Blüthgen, N., & Heethoff, M. (2018). An automated device for the digitization and 3D modelling of insects, combining extended-depth-of-field and all-side multi-view imaging. *ZooKeys*, *2018*(759), 1–27. https://doi.org/10.3897/zookeys.759.24584

[16] Nocerino, E., Menna, F., Remondino, F., Beraldin, J. A., Cournoyer, L., & Reain, G. (2016). Experiments on calibrating tilt-shift lenses for close-range photogrammetry. *International Archives of the Photogrammetry, Remote Sensing and Spatial Information Sciences – ISPRS Archives*, *41*, 99–105. https://doi.org/10.5194/isprsarchives-XLI-B5-99-2016

[17] De Chiffre, L., Carmignato, S., Cantatore, A., & Jensen, J. D. (2009). Replica calibration artefacts for optical 3D scanning of micro parts. In *9th International Conference of the European Society for Precision Engineering and Nanotechnology, EUSPEN*, Spain, 352–355.

[18] Guerra, M. G., Gregersen, S. S., Frisvad, J. R., De Chiffre, L., Lavecchia, F., & Galantucci, L. M. (2020). Measurement of polymers with 3D optical scanners: evaluation of the subsurface scattering effect through five miniature step gauges. *Measurement Science and Technology*, *31*(1), 015010. https://doi.org/10.1088/1361-6501/ab3edb

[19] Guerra, M. G., De Chiffre, L., Lavecchia, F., & Galantucci, L. M. (2020). Use of miniature step gauges to assess the performance of 3D optical scanners and to evaluate the accuracy of a novel additive manufacture process. *Sensors (Switzerland)*, *20*(2). https://doi.org/10.3390/s20030738

[20] Guerra, M. G., Lavecchia, F., & Galantucci, L. M. (2020). Artefacts Used for Testing 3D Optical-Based Scanners. In *Lecture Notes in Mechanical Engineering* (pp. 173–189). https://doi.org/10.1007/978-3-030-46212-3_12

[21] Cantatore, A., Angel, J., & De Chiffre, L. (2012). Material investigation for manufacturing of reference step gauges for CT scanning verification. In *12th International Conference of the European Society for Precision Engineering and Nanotechnology, EUSPEN*, Sweden, 129–132.

[22] Galantucci, L. M., Pesce, M., & Lavecchia, F. (2015). A stereo photogrammetry scanning methodology, for precise and accurate 3D digitization of small parts with sub-millimeter sized features. *CIRP Annals – Manufacturing Technology*, *64*(1), 507–510. https://doi.org/10.1016/j.cirp.2015.04.016

[23] Sims-Waterhouse, D., Isa, M., Piano, S., & Leach, R. (2020). Uncertainty model for a traceable stereo-photogrammetry system. *Precision Engineering*, *63*(September 2019), 1–9. https://doi.org/10.1016/j.precisioneng.2019.12.008

[24] Allen, E., & Triantaphillidou, S. (2011). *The Manual of Photography – "Photographic and geometrical optics"*. Taylor & Francis.

[25] Thomson, G. H. (2010). The practical effect of a diffraction-limited image for photogrammetry. *Photogrammetric Record*, *25*(130), 197–200. https://doi.org/10.1111/j.1477-9730.2010.00580.x

[26] Olkowicz, M., Dabrowski, M., & Pluymakers, A. (2019). Focus stacking photogrammetry for micro-scale roughness reconstruction: a methodological study. *Photogrammetric Record*, *34*(165), 11–35. https://doi.org/10.1111/phor.12270

[27] Lavecchia, F., Guerra, M. G., & Galantucci, L. M. (2018). Performance verification of a photogrammetric scanning system for micro-parts using a three-dimensional artifact: adjustment and calibration. *International Journal of Advanced Manufacturing Technology*, *96*(9–12), 4267–4279. https://doi.org/10.1007/s00170-018-1806-3

[28] Percoco, G., Modica, F., & Fanelli, S. (2016). Image analysis for 3D micro-features: A new hybrid measurement method. *Precision Engineering*. https://doi.org/10.1016/j.precisioneng.2016.11.012

[29] Koik, B. T., & Ibrahim, H. (2014). A literature survey on blur detection algorithms for digital imaging. *Proceedings – 1st International Conference on Artificial Intelligence, Modelling and Simulation, AIMS 2013*, 272–277. https://doi.org/10.1109/AIMS.2013.50

[30] Ahn, S. J., Rauh, W., & Recknagel, M. (1999). Geometric Fitting of Line, Plane, Circle, Sphere, and Ellipse. *ABW-Workshop 6, Technische Akademie Esslingen*, Germany.

Prof. Luigi Maria Galantucci
Full Professor in Technologies and Production Systems School of Engineering, Politecnico di Bari since 2000. Head of several laboratories of the DMMM – Politecnico di Bari: *Rapid Prototyping and Reverse Engineering* and the *MICROTRONIC – Micromachining and Micro-measurement*.
Since 1981, he has been involved in several research projects funded by the Italian Minister of Public Education, the Italian Minister of the Scientific and Technological Research, the National Council of the Research, on 3D scanning and measurement of micro-components, Rapid Prototyping, Reverse Engineering, Manufacturing Processes, Process Planning, Computer-Aided Manufacturing, Feature Technology, Non-Traditional Manufacturing, Welding, Heat Treatment, Forming processes simulation, Manufacturing System Analysis and simulation, Biomechanics, Anthropometry.

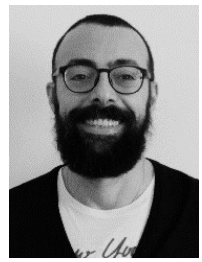

Fulvio Lavecchia
He is Assistant Professor at Politecnico di Bari in the field of Technologies and Production Systems. He collaborates on industrial research projects in the field of Rapid Prototyping and Reverse Engineering. Regarding the Rapid Prototyping, he focuses his interest on Fused Deposition Modelling (FDM) and Fused Filament Fabrication (FFF) technologies for the optimization of the processes and the post treatments for improving the surface finish. He also deals with Reverse Engineering, and in particular, optical digitization techniques, such as Close-Range Photogrammetry, Laser Scanner, Conoscopic Holography also suitable for micro-features analysis.

Prof. Leonardo De Chiffre
Professor Emeritus at the Denmark Technical University. Before, Full Professor and Centre Director, M.Sc., Ph.D., D.Sc., he is an internationally recognized expert in manufacturing and metrology. His theoretical models quantifying the role of friction and lubrication in metal cutting are described in textbooks worldwide. In the field of metrology he has developed calibration methods and artefacts ensuring traceability of measurements on CMM, optical scanners and CT-scanners. He has been initiator and coordinator of major framework programs and created and directed since its formation the *Centre for Geometrical Metrology* (CGM) at the Department of Mechanical Engineering at the Technical University of Denmark (DTU), delivering accredited calibration and testing at the highest level and operating part of the Danish National Primary Laboratory for Length at the Designated Institute DTU (since January 2016 under DFM).

Maria Grazia Guerra
She is a Postdoctoral Researcher at Politecnico di Bari. She has a PhD in Mechanical and Management Engineering in analysis of 3D optical scanning systems applied to reconstruction of small objects and micro-feature, dealing with the challenges characterizing those techniques for a metrological implementation. She is currently working on innovative manufacturing processes and materials, and on the implementation of optical scanners for metrological applications as well as for in situ monitoring of additive fabrication processes.